Position-dependent stability and lifetime of the skyrmion state in nickel-substituted Cu_2OSeO_3

M. Crisanti [1,2,*] M. T. Birch [3], M. N. Wilson,[3] S. H. Moody,[3] A. Štefančič,[2] B. M. Huddart [3], S. Cabeza [1], G. Balakrishnan,[2] P. D. Hatton,[3] and R. Cubitt[1]

[1]*Institut Laue-Langevin, 71 avenue des Martyrs CS 20156, 38042, Grenoble, Cedex 9, France*
[2]*University of Warwick, Department of Physics, Coventry CV4 7AL, United Kingdom*
[3]*Centre for Materials Physics, Durham University, Durham DH1 3LE, United Kingdom*

We report spatially resolved small-angle neutron-scattering measurements of the conical and skyrmion states of a bulk single crystal of nickel-substituted Cu_2OSeO_3, with a nominal concentration of Ni of 14%. We observe a significant spatial dependence of the structure of these magnetic states, characterized by increased disorder and misalignment with respect to the applied field as we approach the edge of the sample. Remarkably, the edge skyrmion state is also characterized by an extended stability towards lower temperatures. Surprisingly, in the same region of the sample, the metastable skyrmion state did not show simple decay. Instead, only a fraction of the scattered intensity appeared to decay, and the intensity therefore did not approach zero during our measurements. We suggest that the increased local disorder and the coexistence of conical and skyrmion states, induced by demagnetization effects at the edge of the sample, are responsible for the increased stability of this skyrmion state. We also infer that the unclear metastable behavior of the skyrmion lattice at the edge of the sample is due to the local geometry of the sample, which induces coexistence of different skyrmion states whose lifetimes are superimposed and difficult to separate in the data.

I. INTRODUCTION

Magnetic skyrmions constitute a topological state of matter that is currently the focus of great research efforts due to their potential application in spintronic devices [1,2]. A skyrmion is a topologically stable, nanosized spin whirl. Its stability arises from the difference between the topological charge of this spin structure ($N = 1$) from neighboring topologically trivial structures that have $N = 0$ [3–5].

Magnetic skyrmions were first observed in the noncentrosymmetric chiral magnet MnSi by means of small-angle neutron scattering (SANS) [6]. Soon after, they have been observed in other materials belonging to the same space group, $P2_13$, such as $Fe_{1-x}Co_xSi$ [7], FeGe [8], and Cu_2OSeO_3 [9], where the lack of inversion symmetry and thermal fluctuations plays a major role in their stabilization [7–9]. Magnetic materials crystallizing in the $P2_13$ space group host the Dzyaloshinskii-Moriya interaction (DMI), responsible for canting neighboring spins. The interplay between the ferromagnetic exchange interaction, the DMI, and the magnetic anisotropy provides these materials with an **H-T** phase diagram characteristic of this set of materials. More recently, skyrmions have been observed in another set of chiral materials, the Co-Zn-Mn family of alloys, where they are stable at room temperature [10]. Skyrmions have also been observed in thin films [11–13], and in centrosymmetric materials [14,15] where magnetic frustration is responsible for the stabilization of this topologically nontrivial spin texture.

In Cu_2OSeO_3, the parent compound of $(Ni_xCu_{1-x})_2OSeO_3$ which is the object of our study, below the ordering temperature T_C, the zero magnetic field ground state is a helical ordering of the magnetic moments, a result of competition between the ferromagnetic exchange and the DMI. In this compound, the helical ground state consists of three domains of helices with their propagation vectors pinned along the [100], [010], and [001] crystallographic directions. When increasing the applied magnetic field at base temperature, the system passes into a single-domain conical state, where the propagation vector lies parallel to the applied magnetic field. Eventually, increasing the field further, the system transitions into a uniform magnetization state.

However, at higher temperatures near T_C the behavior is different. In this narrow region of the **H-T** phase diagram just below T_C, the skyrmion state is stabilized by thermal fluctuations. Here, in what is commonly referred to as the skyrmion pocket, skyrmions arrange in a hexagonal lattice (SkX) and extend along the direction of the applied magnetic field as tubes [16].

Different approaches have been investigated to engineer the size and position of the skyrmion pocket, such as the application of electric fields [17–19], the application of uniaxial [20–22] and hydrostatic pressure [23–27], and the reduction of the sample dimensions into thin films [28]. In addition, it has been shown that it is possible to stabilize the skyrmion state over a wide temperature and field range via rapid field cooling (RFC) through the skyrmion pocket [17,18,29–32]. With this process a metastable skyrmion state is formed over a wide temperature range, that decays into the conical (or helical) state with a temperature-dependent lifetime [18,29].

*Corresponding author: m.crisanti@warwick.ac.uk

It has further been shown that the position of the skyrmion pocket can be tuned through controlled chemical substitution [33–35]. In Cu_2OSeO_3, the substitution of Cu ions with non-magnetic Zn ions led to a shift of the whole phase diagram towards lower temperatures [33]. On the other hand, magnetic doping with Ni induced an increase of the size of the skyrmion pocket towards lower temperatures with increasing Ni substitution, reported for polycrystalline samples studied with both ac susceptibility [34] and SANS [35].

In bulk materials, most of the techniques used to study the skyrmion state provide information that is averaged across the whole sample. However, since the skyrmion state is characterized by a long periodicity, we might expect there to be variations in its behavior across different areas of a bulk sample, which have not been well investigated. Techniques such as SANS, when used in cooperation with a suitable aperture at a high-brilliance source, can provide insight at specific areas of the sample [36]. The often small dimensions of the samples studied represent a major limitation for the acquisition of sufficiently spatially resolved information.

For this reason we focused our study on an exceptionally large single crystal of Ni-substituted Cu_2OSeO_3 with a nominal concentration of Ni of 14% ($6 \times 3 \times 3$ mm^3, 225 mg). The large size of the crystal enabled the study of the spatial variation of the skyrmion magnetic texture and its metastability.

We report spatially resolved small-angle neutron scattering and neutron diffraction measurements performed on a single crystal of Ni-substituted Cu_2OSeO_3. The features of the skyrmion magnetic texture have been mapped across the sample, revealing substantial differences in its structure, its stability, and metastability in areas of the sample only ~ 2 mm away from each other.

II. METHODS

A. Small-angle neutron scattering

A single crystal of Ni-substituted Cu_2OSeO_3 ($6 \times 5 \times 3$ mm^3, 225 mg) with a nominal Ni concentration of 14%, and a pristine Cu_2OSeO_3 ($2 \times 1.5 \times 2$ mm^3, 21 mg) single crystal were both studied with SANS on D33 at the Institut Laue-Langevin (ILL). Both samples were grown by chemical vapor transport [33]. The samples were mounted inside a helium cryostat with a [110] crystal axis along the direction of the neutron beam, and a [1$\bar{1}$0] axis vertical, perpendicular to the neutron beam. Both samples were glued on a 200-μm-thick aluminum plate. Cadmium strips were placed aside of the top and bottom edges of the samples to block the neutrons missing the sample and to help with its vertical alignment to the neutron beam. The magnetic field was applied both parallel and perpendicular to the neutron beam, as shown in Figs. 1(a) and 1(b). Its direction relative to the neutron beam was determined using scattering from the lattice of superconducting vortices in Nb, known to follow the applied field direction [37]. All the measurements were performed with a collimation length of 7.8 m before the sample, and a neutron wavelength $\lambda = 6$ Å, with a full width at half maximum (FWHM) fractional spread of $\Delta\lambda/\lambda = 10\%$. The scattered neutrons were detected 7.8 m after the sample with a two-dimensional multidetector.
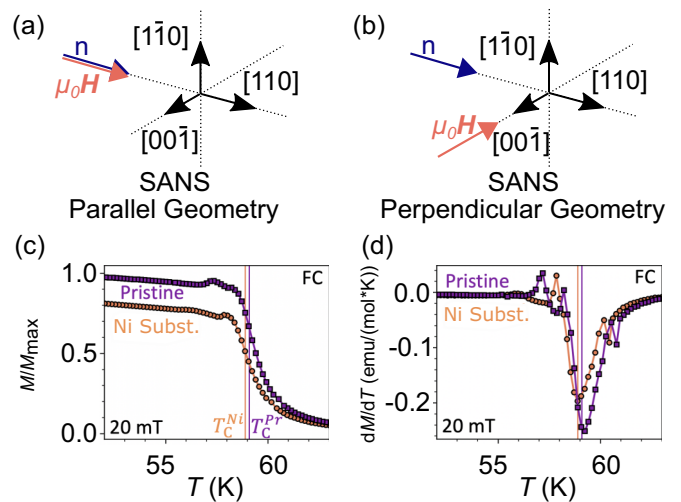

FIG. 1. (a),(b) Schematic of the two SANS experimental geometries. (c) Magnetization measured as a function of decreasing temperature with an applied magnetic field of 20 mT for the pristine (purple squares) and Ni-substituted (orange circles) sample. (d) The calculated gradient of the magnetization with temperature. The minima of this data were used to define T_C, indicated by the colored vertical lines in both panels.

Rocking curves of the conical and skyrmion states were collected by rotating the sample and cryomagnet together around the vertical axis (sample [1$\bar{1}$0] axis), obtaining the intensity of the horizontal magnetic diffraction spots as a function of rocking angle ω. The rocking angle $\omega = 0$ corresponded to the applied magnetic field lying parallel to the incoming neutron beam, and was calibrated by centering the scattering from the flux lines lattice in superconducting Nb [37]. The Ni-substituted sample was studied with two different neutron beam apertures: one of 6 mm diameter, illuminating the whole sample, and a second one of 1 mm diameter, illuminating specific areas of the sample chosen by horizontally translating the magnet and the sample relative to the neutron beam. The pristine sample was studied with a 3-mm aperture, illuminating the whole sample. For the Ni-substituted sample, the phase diagram of the fully illuminated sample was measured by zero field cooling (ZFC) to target temperatures and performing field scans at each temperature [Fig. 3(a)]. The phase diagrams relative to the specific areas of interest on the sample were measured by high field cooling (HFC) in 50 mT, setting a target H, and performing increasing temperature scans at each target field. In both cases the measurements were not affected by metastability, and they represent the true extent of the equilibrium skyrmion state at those specific conditions.

The lifetime of the metastable skyrmion state was measured in both areas of interest on the sample. To perform these measurements, the rocking angle corresponding to the peaks of the rocking curves in the equilibrium state was identified in both areas. The lifetime measurements were then performed by collecting single diffraction patterns at the corresponding rocking angle in each area. All lifetime measurements were performed by field cooling the sample from 70 K to the desired temperature at a rate of 7 K/min.
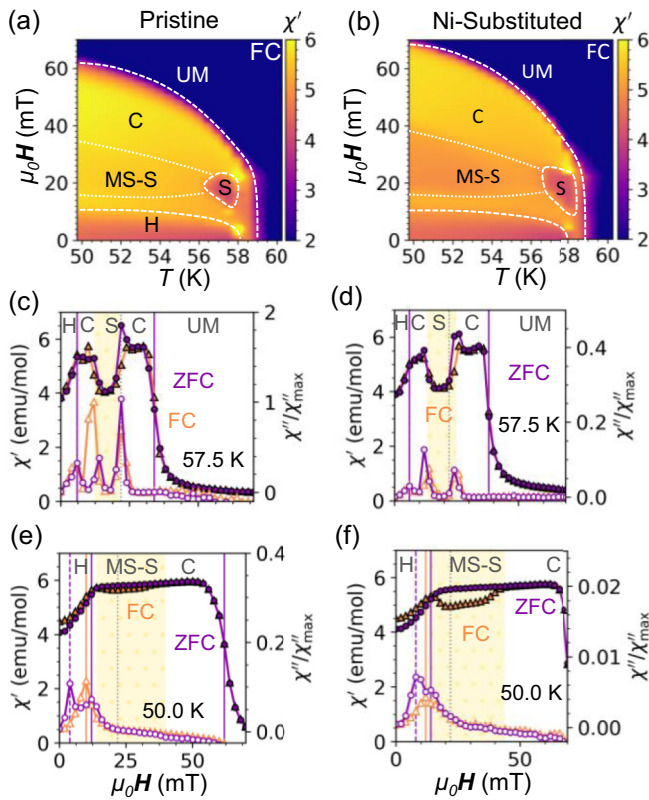
FIG. 2. (a),(b) Magnetic phase diagrams of the pristine and Ni-substituted samples, respectively. The color map plots the real component of the ac susceptibility, χ', as a function of temperature and applied magnetic field. The ac susceptibility measurements at (c),(d) 57.5 K and (e),(f) 50.0 K following the ZFC (purple circles) and FC in 22 mT (orange triangles) are plotted as a function of the applied field for the (c),(e) pristine and (d),(f) substituted samples. The real and imaginary components are denoted by the solid and open markers, respectively. Vertical lines indicate phase boundaries determined by features in the χ'' data, which was normalized to the highest value of χ'' of the pristine sample at 57.5 K. All the helical (H), conical (C), skyrmion (S), metastable skyrmion (MS-S), uniform magnetization (UM), and paramagnetic (PM) states are labeled.

For all SANS measurements we present, paramagnetic backgrounds measured on the same sample at 70 K and 22 mT, with the same aperture and sample positions, were subtracted during the data reduction. The SANS data reduction and analysis was performed using GRASP [38].

B. Neutron diffraction

Neutron diffraction measurements were performed on SALSA, at ILL [39], investigating possible residual strain in the Ni-substituted single crystal. A monochromated neutron beam with a wavelength of 1.7002 Å was collimated to a voxel size of $0.6 \times 2 \times 0.6$ mm^3. The sample was mounted with the [110] crystallographic direction in the scattering plane and the [1$\bar{1}$0] perpendicular to it. The sample was then rotated around its vertical axis to meet the Bragg condition of the (044) plane at the detector position of $2\theta = 65.5°$. This Bragg reflection was measured across the sample, with an acquisition time of 10 s per point, mapping its intensity, and any variation of 2θ,
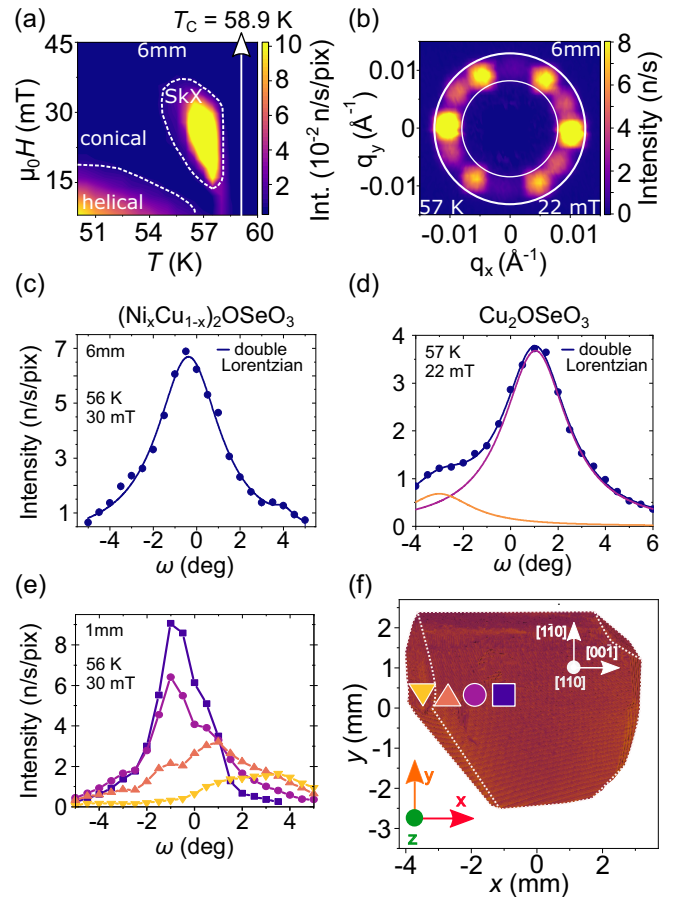

FIG. 3. (a) SANS **H-T** phase diagram of the Ni-substituted sample, derived by summing the scattered neutron intensity in the region of the detector between the two white circles indicated in (b). The dashed lines serve as a guide to the eye to identify the boundaries between the various magnetic phases in the sample. The solid white vertical line indicates the value of T_C measured with ac susceptibility (Fig. 1). (b) Typical skyrmion lattice scattering pattern recorded using a 6-mm aperture that fully illuminated the Ni-substituted sample at 22 mT and 57 K. (c) Mid-pocket rocking curve of the equilibrium skyrmion state of the Ni-substituted sample. (d) Mid-pocket rocking curve of the pristine sample. Both data sets in (c) and (d) fit to the sum of two Lorentzian functions (dark blue), that are singularly shown in purple and orange in (d). (e) Rocking curves recorded in the equilibrium skyrmion state with a 1-mm aperture at different positions on the Ni-substituted sample. Each rocking curve was measured translating horizontally in steps of 0.5 mm on the sample surface indicated in (f). (f) X-ray tomography of the surface of the sample struck by neutrons during the SANS experiment. The dashed white lines are a guide to the eye and identify the edges between adjacent surfaces. The symbols are a guide to the eye to identify the positions at which each of the rocking curves in (e) were measured.

and hence any change in the crystal lattice parameter to a precision of 10^{-4}. To ensure the correct mapping of the edge of the sample, in this region the measurements were performed in steps of 0.2 mm, smaller than the size of the beam, and then recombined to take into account the partially illuminated areas of the sample when hitting its edge. The measurements were performed at room temperature and zero applied magnetic field, and at 56.0(1) K and 22 mT. The data were reduced and

analyzed with the Large Array Manipulation Program (LAMP) software [40].

The characterization of the single-crystal structures and the alignment of the samples were performed on the OrientExpress Laue diffractometer at ILL [41], for both the Ni-substituted and pristine samples. The single crystals were mounted on a two-stage tilt goniometer, and illuminated with a white neutron beam. The scattering patterns were collected with an average of 20 s exposure time on a charged coupled device sensor, coupled to a scintillator, in backscattering geometry.

C. Magnetometry

dc and ac magnetometry measurements were performed using an MPMS3 Quantum Design superconducting quantum interference device (SQUID) magnetometer. Using GE varnish, the single-crystal samples were fixed to a quartz rod with the [110] crystal axis parallel to the applied magnetic field. The ac susceptibility measurements were undertaken at a frequency of 10 Hz, and with a field amplitude of 0.1 mT. A rate of 40 K/min was set for all cooling procedures. Magnetization versus temperature measurements determined T_C to be 59.1(1) K for the pristine sample and 58.9(1) K for the Ni-substituted sample, as shown in Figs. 1(c) and 1(d).

D. X-ray tomography

The sample volume and shape were studied with x-ray tomography measurements performed on the NeXT-Grenoble (ILL) [42] instrument at room temperature and zero magnetic field. A polychromatic x-ray beam at 120 kV and 60 μA was collimated to a voxel size of 20 μm. A tin filter of 500 μm was added to cut low wavelengths, producing an x-ray beam peaking at 50 keV. The sample was mounted on a rotation stage. Transmission images were recorded as a function of sample rotation until the sample was fully illuminated. The tomography resulted in 1312 images, each one recorded as an average of seven single frames, each one with an exposition of 0.3 s.

E. Density functional theory calculations

To determine the Young's modulus of Cu_2OSeO_3, we used the plane-wave basis-set electronic structure code CASTEP [43] and worked within the generalized-gradient approximation (GGA) using the Perdew-Burke-Ernzerhof (PBE) functional [44]. We used a plane-wave cutoff energy of 1000 eV and a $5 \times 5 \times 5$ Monkhorst-Pack grid [45] for Brillouin zone sampling, resulting in stresses that converged to 0.1 GPa. Elastic constants were obtained by applying a series of strains to the unit cell and calculating the corresponding stresses.

III. RESULTS

A. Ni substitution effects on the whole sample

Figures 2(a) and 2(b) display the real component of the ac susceptibility measurements, χ', for the pristine and Ni-substituted samples, respectively. χ' was measured field cooling (FC) in 22 mT at selected target temperatures between 49 and 61 K, and then measuring increasing field. The system

was then reset and field cooled again in 22 mT to the same target temperatures, then measuring decreasing field. The same procedure was utilized on both the pristine and Ni-substituted samples. Features in the data were used to determine the magnetic phase diagram. The lower value of χ' close to 0 mT is a signature of the helical state, while the lower valued region at $\approx$20 mT and 58 K indicates the formation of the skyrmion lattice state [46].

These features are more easily seen in Figs. 2(c) and 2(d), which plot the measured value of χ', at 57.5 K against the applied field. Comparison of the data suggests little difference in the response of the pristine and Ni-substituted samples at this temperature. These panels also plot the imaginary component, χ''. At this temperature, the peaks in χ'' are associated with energy losses due to excitations at the magnetic phase boundaries between the helical and conical and the skyrmion and conical states [46]. The values of the imaginary component were normalized to the highest measured value of χ'' in the pristine sample, at 57.5 K, in order to allow for comparison of the χ'' signal between the two samples.

The χ' data in Figs. 2(a) and 2(b) also display a broad reduction in the χ' value around 20 mT across all temperatures, demonstrating the formation of a metastable skyrmion state. The ZFC and FC data for both samples at 50 K shown in Figs. 2(e) and 2(f) demonstrate that the value of χ' after field cooling is reduced to a greater extent in the Ni-substituted sample compared to the pristine. This indicates that a larger population of metastable skyrmions is formed in the Ni-substituted sample, suggesting that the Ni substitution has increased the metastable skyrmion lifetime in a manner similar to that seen in Zn-substituted Cu_2OSeO_3 [29].

Turning now to the imaginary component at 50 K, shown in Figs. 2(e) and 2(f), we see that the magnitude of the peaks are reduced in the Ni-substituted sample. Similar behavior was previously reported in a Zn-substituted sample, where it was attributed to pinning effects introduced by the dopant [47]. Furthermore, there are two peaks seen in the ZFC data for both samples. These have previously been attributed to the reorientation of different helical domains in the Cu_2OSeO_3 when the field is applied along the [110]. Significantly, our data suggest that this reorientation occurs in both the Ni-substituted and pristine samples, while it has been reported that this feature is suppressed by Zn substitution [47]. This suggests that the magnetic Ni substitution modifies the phase transitions in Cu_2OSeO_3 in a different manner compared to nonmagnetic Zn substitution.

IV. SKYRMION LATTICE STRUCTURE

The equilibrium skyrmion pocket of the Ni-substituted sample was also measured with SANS and is reported in Fig. 3(a). These measurements are consistent with the magnetometry results of Fig. 2(b), which showed that the skyrmion pocket in the chemically substituted single crystal was enlarged compared to the pristine single crystal in Fig. 2(a). This was also previously reported for polycrystalline samples of Ni-substituted Cu_2OSeO_3 [34,35]. SANS allowed the characterization of the ordering of the different magnetic states in our Ni-substituted sample. The skyrmion lattice was characterized

by the typical six-fold scattering pattern shown in Fig. 3(b), while both the conical and helical states were characterized by two horizontal diffraction spots. The momentum transfer, or **q**, of the skyrmion state was $q_{SkX} = 0.0103(1)$ Å^{-1}, the same value, within experimental uncertainty, as that of the helical state, $q_h = 0.0104(1)$ Å^{-1}. The corresponding characteristic spacing of the skyrmion lattice was $d_{SkX} = \frac{2\pi}{q_{SkX}} \simeq 607(8)$ Å, in agreement with previously published work on the pristine and Zn-substituted samples [9,29].

Rocking curves of the horizontal diffraction spots were measured in the center of the skyrmion pocket for both the Ni-substituted and pristine samples and are reported in Figs. 3(c) and 3(d), respectively. In both cases, the data fit well to the sum of two Lorentzian functions, indicating the presence of two skyrmion domains characterized by different mean directions away from the applied magnetic field, and by different spreads of angles. These domains are present in addition to the azimuthally rotated domain by 30° observed on the detector plane in Fig. 3(b), since they lie in the plane perpendicular to the detector. In order to ascertain how the multiple skyrmion domains were distributed within the sample, a 1-mm aperture of the neutron beam was utilized to selectively study specific areas of the sample and spatially resolve its magnetic features.

Figure 3(e) shows rocking curves collected in the equilibrium skyrmion pocket with the 1-mm aperture, at different positions across the horizontal axis of the Ni-substituted sample, as indicated by the colored markers in Fig. 3(f). The mean alignment of the skyrmion tubes and their distribution dramatically changes with each 0.5-mm step. Higher tilting angles were observed when illuminating the edge of the sample, while skyrmion domains better aligned to the direction of the applied field were observed towards the center of the sample.

To further investigate the spatial dependence of the skyrmion and conical structure, a detailed set of rocking curves was collected across the sample on the line formed by the symbols in Fig. 3(f), and their analysis is reported in Fig. 4. Here a three-dimensional representation of each rocking curve is given at each different position on the sample, allowing the visualization of this complex picture of tilting domains: the length, width, and orientation of the cones indicate the fitted maximum intensity, FWHM, and peaking angle of the rocking curves.

The conical state was measured at 50 K at both 8 and 30 mT, as reported in Figs. 4(a) and 4(b), respectively. The magnetic field was applied along the [001] crystal axis, perpendicular to the incoming neutron beam. The typical pair of horizontal diffraction spots characterizing the conical state were visible on the detector in both field conditions. At low field, multiple peaks were observed in the rocking curves, shown by the multiple cones present in some areas of the sample, indicating multiple conical domains tilting away from the direction of the applied magnetic field. When increasing the field to 30 mT, the multidomains were suppressed in favor of single peaking rocking curves varying smoothly across the sample. At this higher field, the dominant domains tilt away from the field direction in similar directions to that seen at 8 mT; however, the size of this tilting angle is generally increased, especially at the edges of the sample.

Figure 4(c) reports the detailed scan across the sample of the skyrmion state. The right side of the sample was characterized by multiple domains visible both on the detector plane as multiple sets of six-fold scattering patterns and in the rocking curve profiles, characterized by multiple peaks. The left side of the sample was instead characterized by a single skyrmion domain visible on the detector plane. On this side of the sample, it was possible to observe that the tilting angles increased at the edge compared with the center. The skyrmion domains were tilting strongly up to an angle of ±4° away from the applied magnetic field direction, compared with the thinner and more aligned rocking curves measured in the center.

The increased tilting of the conical domains at the edges of the sample compared to its center shows a difference in the alignment of the magnetic texture between the edges and center of the sample. This indicates the influence of a strong demagnetization effect linked to the complex shape of our single crystal. A similar effect was previously observed on the skyrmion state in MnSi and attributed to demagnetization fields [36], consistent with our observations.

V. EQUILIBRIUM SKYRMION REGION

In this complex map of the skyrmion state, two regions of the sample were chosen to concentrate on, hosting two different skyrmion states, marked in Fig. 4(c) by a purple square and a yellow triangle, and shown in detail in Fig. 5. The first region was situated towards the center of the sample, where the main component of the rocking curve was mostly aligned to the applied field, which corresponded to a rocking curve peaking at $\omega = 0.65(5)°$, as shown in Fig. 5(a). The second region, situated towards the edge of the sample, was characterized by two skyrmion domains, strongly tilted away from the direction of the applied magnetic field, with mean angles $\omega_1 = -3.5(1)°$ and $\omega_2 = -1.2(1)°$, as shown by the two fitted peaks in Fig. 5(b). These two areas were chosen as they represented the main features of the rocking curve measured when illuminating the whole sample, where the first region corresponded to its main peak at $\omega \approx -1°$, while the second one is to its left shoulder at $\omega \approx 3.5°$, as shown in the double fit in Fig. 3(a). We refer to these two regions of the sample as "center" and "edge."

Remarkably, in addition to the differences in rocking curves already discussed, these two regions displayed skyrmion pockets extending over significantly different regions in magnetic field and temperature, as shown in Figs. 5(c) and 5(d). The central skyrmion domain existed over a similar area of the **H-T** phase diagram to the one identified illuminating the whole sample [Fig. 1(a)]. The edge skyrmion domain, however, showed a much wider region of stability: it extended twice as much in temperature (from 54 to 58 K), while the field range remained similar to the central skyrmion domain.

The graphs in Figs. 5(e) and 5(f) were produced by recording the skyrmion scattered intensity at $\omega = -0.65°$ in the center position, and at $\omega = 3.1°$ at the edge position, in three horizontal scans across the sample, performed at at $y = -1$, 0, and 1 mm. These two panels show the presence of these two specific skyrmion domains across the sample. The edge skyrmion domain was principally located on the left side of
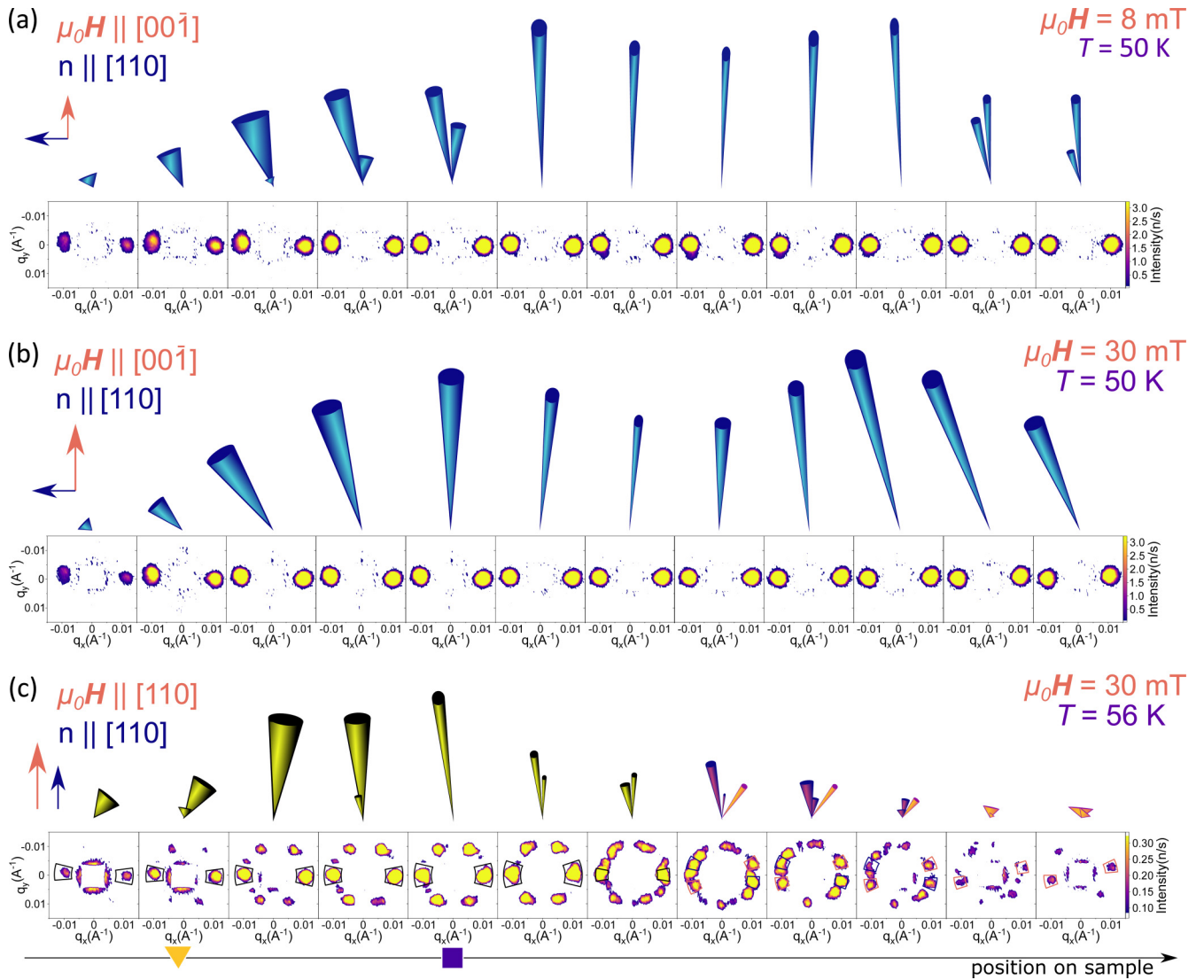
FIG. 4. (a),(b) Scattering patterns of the conical state at 30 mT and 8 mT, 50 K, collected across the sample surface in steps of 0.5 mm. (c) Scattering patterns of the skyrmion state at 30 mT, 56 K, collected across the sample surface in steps of 0.5 mm. In each case, the rocking curves of the horizontal spots in the scattering patterns were analyzed, and their characteristics are displayed by the cones above the scattering patterns. The rocking curves were fitted to a suitable combination of Lorentzian functions: each cone corresponds to one of these functions. Where multiple cones are present, the rocking curves were characterized by multiple peaks, and hence fitted to the sum of multiple Lorentzian functions. The intensity of the fitted curves is proportional to the height of the cones, and in the skyrmion case this height was multiplied by 10 compared to that of the cone phase. The FWHM of the fitted curves is proportional to the width of the cones, in the range from $0.3°$ to $5°$. The center of the fitted curves is proportional to the tilting angle of the cones, in a range going from $-4°$ to $+4°$. The direction of the applied field and the neutron beam are reported in the top left of each panel. Where multiple domains were visible in the scattering patterns of the skyrmion state, the pairs of spots analyzed were boxed and color coded in the same way as the corresponding cones. The symbols on the line at the bottom correspond to the positions noted in Fig. 3(f).

the sample, where we found the widest rocking curves and the highest average tilts away from the applied magnetic field direction.

The differences in the alignment of the skyrmion lattice between the edge and the center of the sample, and the localized presence of the edge domains, are consistent with demagnetization effects [36] linked to the complex shape of the sample shown in Fig. 6(b). In particular, we note that a measured cavity inside the sample, which would not have been identified without x-ray tomography measurements, significantly affects the behavior between $x = 0$ and 2 mm, corresponding to the

right side of the scan in Fig. 4(c). However, we note that while demagnetization effects could cause a small shift in the magnetic field position of the skyrmion pocket at different points in the sample, they cannot directly explain the substantial enhancement of the temperature range of the skyrmion pocket that we observed. This led us to consider other possible explanations for this effect.

One possibility could be differences in strain across the sample, which is known to modify the temperature extent of the equilibrium skyrmion region [20–22]. This led us to investigate possible residual strain present in the sample.
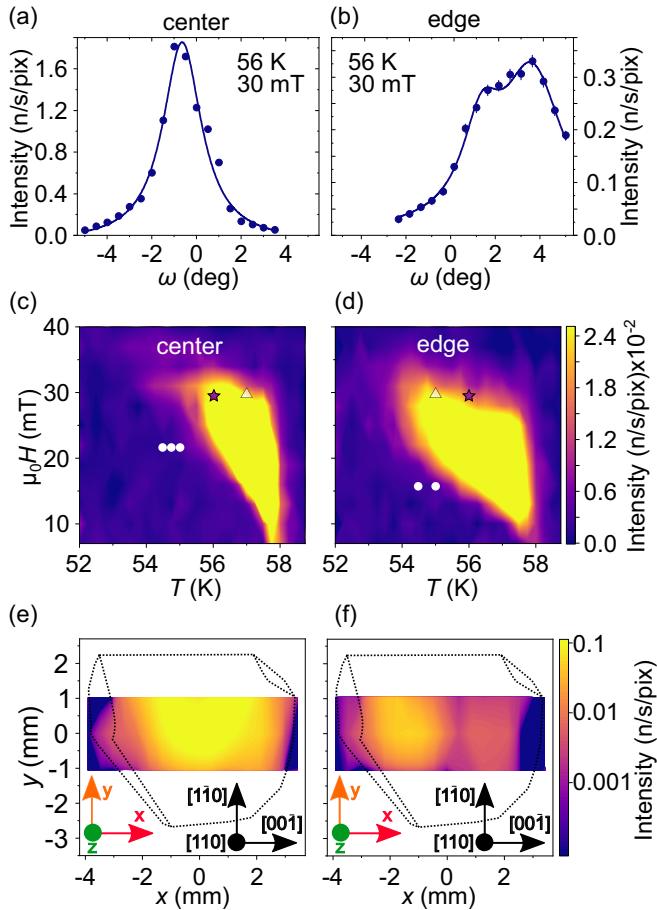
FIG. 5. (a),(b) Mid-pocket rocking curves collected towards the center of the sample and at its edge, respectively, showing the differently oriented skyrmion domains. (c),(d) Phase diagrams measured in the two areas of interest of the sample. The white dots in the diagrams correspond to the H-T parameters at which the lifetime of the metastable skyrmion state was measured in each area. The stars indicate the point at which the rocking curves in (a) and (b) were measured. The white triangles indicate the H-T conditions under which the graphs in (e) and (f) were measured. (e),(f) Neutron-scattered intensity, in logarithmic scale, across the sample of the aligned (centered) skyrmion domain and misaligned (edge) one, respectively. The map was constructed interpolating three horizontal scans performed with 1-mm aperture at three different y positions, in steps of 1 mm. These panels represent the presence of each of the two domains across the sample.

We used neutron diffraction to measure the strain across the sample at room temperature and at 56 K in a field of 22 mT. For these measurements, we tracked the intensity and angular position of the (044) Bragg reflection across the sample. We first performed a rocking curve of this peak in the center of the sample to identify the angle of the (044) peak (FWHM $\approx 1°$), and then scanned across the sample at this fixed angle to map the peak intensity. These data are shown in Fig. 6(a).

The intensity variation across the sample was due to two factors. First, due to the narrow rocking curve width, a decrease in the intensity of this reflection could arise from a change in the rocking curve width, in its mean direction, or both. However, a measurement of neutron Laue scatter-
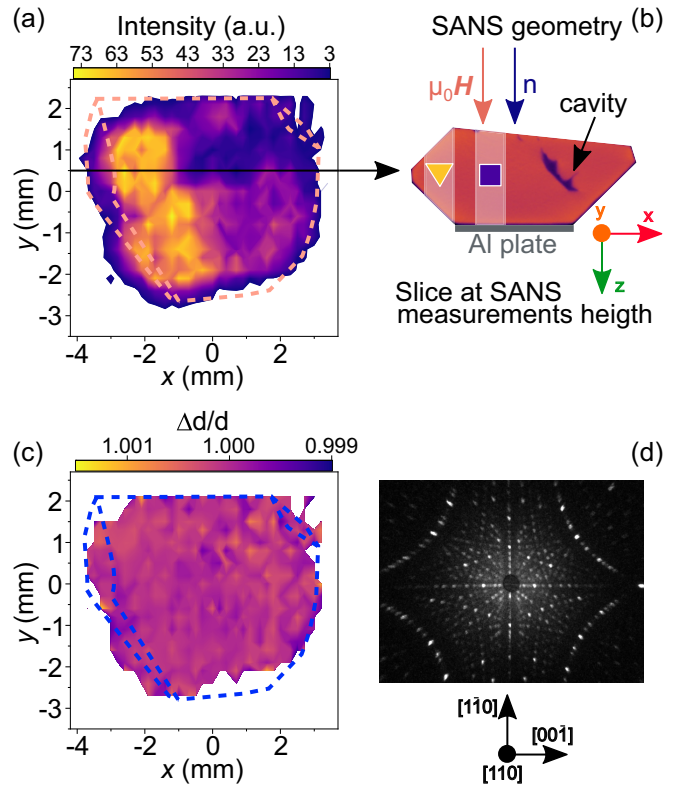

FIG. 6. (a) Map of the intensity of the (044) Brag peak. (b) Mid-height slice of sample in the x-z plane derived from x-ray tomography. Both the neutron beam and the magnetic field direction are indicated and refer to the geometry of the SANS experiment. A cavity is visible on the right side of the sample. The shaded areas marked with the yellow triangle and the blue square refer to the positions of the edge and central skyrmion domains, respectively. (c) Fractional variation of the crystal lattice d spacing across the sample. (d) Neutron Laue image of the sample.

ing illuminating the entire sample showed no defects and a single-crystal structure [Fig. 6(c)]. For this reason, possible variations of mosaic spread were only on the scale of a fraction of a degree. Second, the irregular sample shape combined with the small cavity observed with x-ray tomography [Fig. 6(b)] meant that in different positions, different sample volumes were illuminated, which we believe was the dominant contribution to the intensity variation of this Bragg reflection across the sample.

Of primary interest was the variation of the fitted 2θ position of the Bragg reflection on the detector, hence the d spacing of the (044) planes. To a precision of 10^{-4} we could map the fractional variation of the d spacing as a function of position in the sample at 56 K, 22 mT, reported in Fig. 6(b). The distribution of the d-spacing variation was flat, indicating no variation of residual strain in any area of the sample when in the skyrmion equilibrium conditions. Only a 0.09% difference was observed between the room-temperature, zero magnetic field measurement and the 56 K, 22 mT measurement, consistent with the thermal contraction expected for this material [48], which suggests the absence of strain induced by the magnetism below T_C.
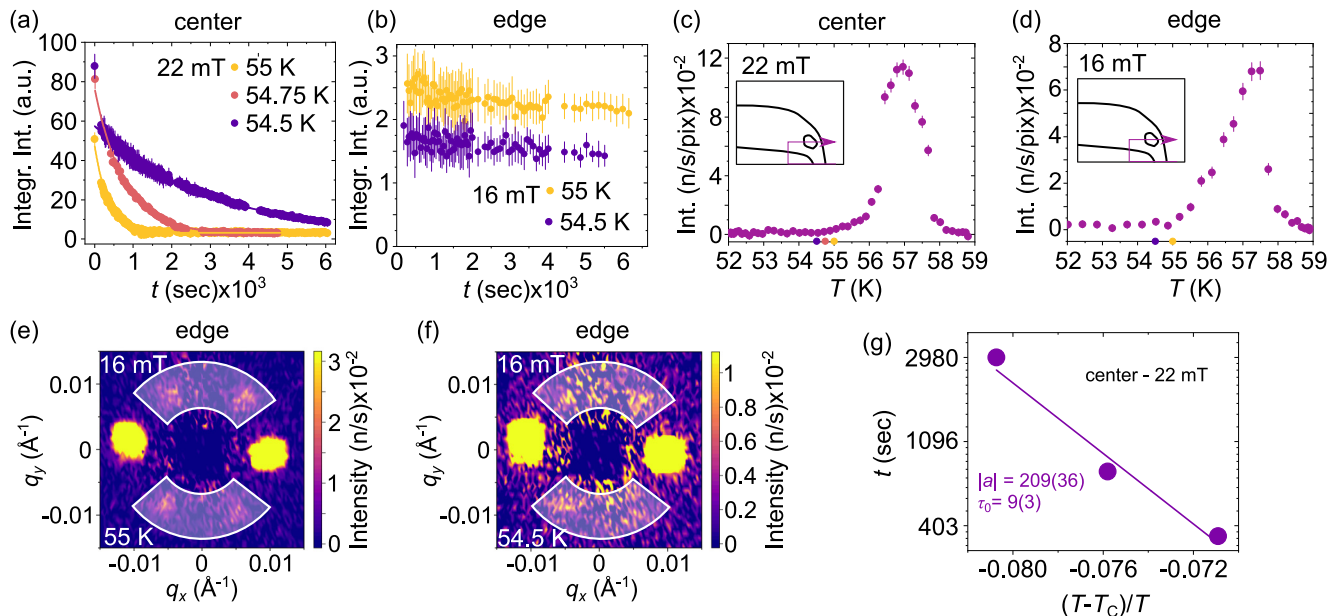
FIG. 7. (a) Lifetimes measured in the center of the sample, FC in 22 mT to 55, 54.75, and 54.5 K. (b) Lifetimes measured at the edge of the sample, FC in 16 mT to 55 and 54.5 K. The solid lines in (a) indicate the exponential decay fit of the data. (c),(d) Field warming scans performed in the center and on the edge of the sample, respectively. In each panel the history of the measurement is indicated in the inset. The target temperatures of the lifetimes in (a) and (b) are marked on the temperature axis. (e),(f) Sum of scattering patterns of full rocking scans performed ~4000 s after the beginning of the lifetime measurements of the edge metastable skyrmion state at 55 and 54.5 K, respectively. The shaded areas highlight the parts of the detector where it was possible to observe scattering from the skyrmion lattice. (g) Arrhenius plot for the lifetime fits in (a). The data were fitted to a modified Arrhenius-like law. From the linear fit of the data the activation energy parameter a and the attempt time τ_0 were extracted.

It has been previously shown that on Cu_2OSeO_3 a stress on the order of 100 MPa induced an extension of the skyrmion pocket comparable with what we observed in our measurements [22]. In order to correlate a change in the lattice parameter, which we measured, with the stated applied uniaxial pressure, that was previously reported, we calculated the Young's modulus of Cu_2OSeO_3 using density functional theory to be 67(9) GPa. Assuming a stress of 100 MPa to obtain the enlarged pocket at the edge of the sample, with the calculated Young's modulus we would expect a difference in the d spacing between the central and the edge position of 1.5×10^{-3}, which is well above the sensitivity of our measurements of 10^{-4}. As we did not observe any variation of the lattice parameter on this scale, we can state that strain is not the cause of our expanded skyrmion pocket. We discuss alternate explanations later in this paper.

VI. SKYRMION METASTABILITY

The range of temperatures at which the skyrmion state exists can be temporarily extended by rapid field cooling through the equilibrium pocket [17,31,32] to a target temperature. This procedure creates a metastable skyrmion state present over a wide range of temperatures and magnetic fields, which decays over time into the equilibrium magnetic structure. The characteristics of the metastable skyrmion state and its decay are determined by three major factors: the cooling rate, which determines its population [29], as well as the target temperature [7,17,30–32,49–53] and the disorder of the underlying crystal structure [29], both of which determine its lifetime. We

investigated the differences in the metastable skyrmion states located in the center and on the edge of the sample.

According to previous studies on Cu_2OSeO_3 [18,29], lifetimes of minutes to hours were expected when RFC in 22 mT to 54.5, 54.75, and 55 K. However, in these conditions, it was not possible to create a metastable state at the edge of the sample, since the same target temperatures lie inside the extended skyrmion pocket. In order to rapid field cool to the same target temperatures, and obtain a similar range of lifetimes in both areas of the sample, the applied field was adjusted to 16 mT for the measurements at the edge of the sample. In this way, in both areas of the sample we were able to select the same target temperatures for the cooling process while maintaining comparable distances from the low-temperature edge of the equilibrium skyrmion pocket, which was different in the two areas, hence providing a similar range of lifetimes [29].

The metastable skyrmion state at the center of the sample showed a lifetime that increased with decreasing temperature, as shown in Fig. 7(a), similar behavior to both pristine and Zn-substituted Cu_2OSeO_3 [17,18,29,53]. The lifetimes were determined by fitting the decaying intensity to a single exponential with a background, $I = y0 + I_0 \exp(-t/\tau)$, obtaining $\tau(54.5 \text{ K}) = 2978(56)$ s, $\tau(54.75 \text{ K}) = 768(11)$ s, and $\tau(55 \text{ K}) = 356(5)$ s. The characteristic lifetime was longer than the pristine case [29], as suggested by the ac susceptibility measurements shown in Figs. 2(e) and 2(f).

Remarkably, the edge metastable skyrmion state did not show a clear time dependence at any of the selected target temperatures, as shown in Fig. 7(b). An overall small decay of a fraction of the intensity can be observed in the data

over a long period of time, while the scattered intensity did not approach zero. Moreover, the typical six-fold scattering pattern from the skyrmion lattice was still visible at the end of the lifetime measurements as shown in Figs. 7(e) and 7(f). These observations suggest the presence of an unexpectedly enhanced stability of the edge metastable skyrmion domain; however, given the almost flat time dependence of the scattered intensity, it was not possible to produce an Arrhenius plot for the edge state. Furthermore, no change in the widths of the rocking curves was observed over the decay.

The Arrhenius plot of the lifetime fits for the central skyrmion domains is shown in Fig. 7(g). Similar to Refs. [29,32,49,54], the data were fitted to a modified Arrhenius law, $\tau(T) = \tau_0 e^{\frac{a(T-T_C)}{K_B T}}$, expressing the temperature dependence of the metastable skyrmion state's lifetime in terms of the activation energy of the decaying process. From the fit of the data we extracted the activation energy parameter a and the attempt time τ_0 for both the central and domains. For the central domain $|a| = 209(36)$ and $\tau_0 = 9(3)$ s. These results are comparable with what was reported for the CoZnMn alloys in Ref. [54]. Moreover, an increase in the activation energy parameter a, compared to pristine and Zn-substituted Cu_2OSeO_3 [29], is also observed.

In Figs. 7(c) and 7(d) we show the extent of the skyrmion pocket in the center and at the edge of the sample, and measured field warming after ZFC to 52 K. This demonstrates that the target temperatures chosen for the lifetime measurements, indicated by the colored dots in both panels, were outside the equilibrium region of the skyrmion state both at 22 mT in the central area of the sample, and at 16 mT at the edge.

VII. DISCUSSION

We observed position-dependent characteristics of the skyrmion state which displayed different regions of stability [Figs. 5(c) and 5(d)], significant variations in its metastable behavior [Figs. 7(a) and 7(b)], and a different structure [Figs. 5(a) and 5(b)] between the edge and the center of the sample. Here we discuss possible explanations for such differences.

The structural differences in the skyrmion lattice can be accounted for by demagnetizing effects. The central area of the sample has surfaces almost perpendicular to the applied field, while the edge area presents two surfaces approximately 45° to the applied field direction, as shown in Fig. 6(b). The sample shape determines the demagnetization field, which induces variation in the curvature and strength of the internal field [55]. These variations in the internal field explain the high tilting angles, and wider profiles of both the conical and skyrmion rocking curves at the edges of the sample, as both of these states are expected to align themselves with the local magnetic field direction. This is also supported by the increase of the tilting angles of the conical rocking curves at the edge when increasing the strength of the applied field, as this would accentuate the demagnetization field effects.

It was previously observed in MnSi that the demagnetizing field in a disk-shaped sample induced a broadening and a tilting of the skyrmion domains at the edges, and the skyrmion state nucleated at lower fields in the edge of the sample than the center [36]. Our results on the structure of the skyrmion lattice are largely consistent with this study. However, we did not observe a measurable shift in field position or extent of the skyrmion pocket between the edge and the center. Instead we observed a surprising enlargement of the skyrmion pocket towards lower temperature on the edge of the sample.

The size of the skyrmion pocket in Ni-substituted Cu_2OSeO_3 is strongly dependent on the actual content of Ni in the sample, as shown in Ref. [35]. An uneven distribution of Ni across the sample could lead to areas hosting differently extended skyrmion pockets. However, the increasing Ni content would be accompanied by an increase of the ordering temperature T_C [35], and hence a change in the boundary between the paramagnetic and conical state, which was not observed in this study. The position of this boundary was measured in both the edge and central positions and determined to be the same within uncertainty, ruling out a nonuniform level of Ni substitution across the sample as a possible explanation for the enlarged skyrmion pocket at the edge.

The extension of the skyrmion pocket towards lower temperatures, without the increase of T_C, has been obtained by the application of uniaxial pressure [20–22]. However, as mentioned previously, our neutron diffraction measurements rule out this effect.

Recent Lorentz transmission electron microscopy measurements on FeGe lamellas [56] showed that the decay of the metastable skyrmion state is affected by the local environment of individual skyrmions. Specifically, more isolated skyrmions were found to have a higher energy barrier for the decay into the helical state; hence they were more stable than the ones situated in the interior of the lattice.

As the energetics of a single skyrmion changes according to its relative position to the skyrmion lattice, it is reasonable to assume that the energy landscape of the skyrmion lattice itself can be influenced by the perfection of its local structure. The edge of the sample was characterized by wider rocking curves, with substantially higher tilting angles and multiple peaks, describing multiple neighboring skyrmion lattice domains tilting with respect to each other. On the other hand, the center was characterized by single peaking rocking curves with smaller tilting angles. Furthermore, it has been shown that demagnetization effects induce a coexistence of the skyrmion and conical phase in MnSi in a wide region of the phase diagram [36]. Given the shape of our sample, we expect a wider range of internal magnetic fields, and hence a wider coexistence of the skyrmion and conical phase, at the edge of the sample. In this case, the regularity of the skyrmion lattice is likely interrupted by the presence of the conical phase, where the skyrmions at the border between these two phases have a higher stability than the skyrmions at the interior of the lattice [56]. Interruptions to the regular lattice structure by the rotation between neighboring skyrmion domains may also have a similar effect of increasing the skyrmion stability at these defect sites. These two contributions together may explain the increased temperature range of the equilibrium skyrmion pocket that we observed at the edge of our sample.

It is also worth discussing the absence of a clear decaying behavior of the metastable skyrmions in our measurements of the edge state. First, it is worth noting that there is a known variation of the skyrmion lifetime with applied magnetic field

at fixed temperature, and hence we must consider the effect of the difference in the magnetic field between the edge and center measurements. However, lower fields are generally expected to reduce the metastable lifetime, not increase it [57], so this effect does not explain our observations. Second, as the lifetime of the metastable state is determined by the temperature difference between the target temperature of the cooling and the ordering temperature T_C [32,49,54], and no change in the latter was observed, the same Arrhenius temperature dependence of the lifetime was expected in both areas of the sample. In light of these observations, the unclear time dependence of the metastable intensity at the edge of the sample could arise from the imperfect local geometry of the sample. This would induce the coexistence of several skyrmion states characterized by different metastable behaviors, and possibly different regions of stability. The multiple metastable skyrmion domains with different lifetimes would explain the impossibility of fitting the decaying data with a single decaying exponential, while the presence of stable skyrmion domains would explain the persistent scattered intensity of the skyrmion lattice reported in Figs. 7(e) and 7(f). Further measurements of the metastable lifetime at the edge of the sample would be needed to ascertain the temperature dependence of its lifetime.

VIII. SUMMARY

We have characterized the magnetic states of a bulk single crystal of Ni-substituted and pristine Cu_2OSeO_3 with ac susceptibility and small-angle neutron scattering.

Magnetometry measurements showed a decrease of ∼0.3% of the ordering temperature T_C in the Ni-substituted sample, compared to the pristine one. The Ni substitution also increased the population of the metastable skyrmion state in a similar manner to what was previously seen in Zn-substituted Cu_2OSeO_3 [29].

Spatially resolved small-angle neutron-scattering measurements allowed a detailed study of the ordering of the conical and skyrmion states performed through the analysis of their rocking curves shown in Fig. 4. The ordering of both the conical and skyrmion states was position dependent, characterized by wider rocking curves and higher tilting angles from the

direction of the applied field at the edge of the sample. These position-dependent structural changes of these magnetic textures can be explained by demagnetization effects, tilting the internal field lines according to the complex shape of the sample.

Remarkably, an extension towards lower temperatures of the skyrmion pocket was observed at the edge of the sample, compared to the center. This extension could not be attributed neither to a varying Ni substitution level across the sample, as the conical-paramagnetic boundary is identical at both sample positions, nor to residual strain, as neutron diffraction measurements showed no deformation of the unit cell across the sample. Instead, we link the increased stability of the skyrmion lattice at the edge to the ordering of its local structure. The strong demagnetization effects present at the edge of the sample likely induce coexistence with the conical state [36], and deform the skyrmion lattice, creating irregularities in its structure which affect its metastable lifetime, and also the temperature range of the skyrmion pocket [56].

Our findings underline the important link between skyrmion lattice structure and its stability and metastability. In particular, such effects could be exploited for the engineering of skyrmion devices with specific shapes that would make a nonvolatile skyrmion state available at a wider range of temperatures. It also appears crucial from our findings to account for the demagnetization effect in the interpretation of bulk measurements.

[1] A. Fert, V. Cros, and J. Sampaio, Skyrmions on the track, Nat. Nanotechnol. **8**, 152 (2013).

[2] A. Fert, N. Reyren, and V. Cros, Advances in the physics of magnetic skyrmions and perspective for technology, Nat. Rev. Mater. **2**, 17031 (2017).

[3] U. K. Rößler, A. N. Bogdanov, and C. Pfleiderer, Spontaneous skyrmion ground states in magnetic metals, Nature **442**, 797 (2006).

[4] N. Nagaosa and Y. Tokura, Topological properties and dynamics of magnetic skyrmions, Nat. Nanotechnol. **8**, 899 (2013).

[5] K. Everschor-Sitte, J. Masell, R. M. Reeve, and M. Klaui, Perspective: Magnetic skyrmions - Overview of recent progress in an active research field, J. Appl. Phys. **124**, 240901 (2018).

[6] S. Mühlbauer, B. Binz, F. Jonietz, C. Pfleiderer, A. Rosch, A. Neubauer, R. Georgii, and P. Böni, Skyrmion lattice in a chiral magnet Science **323**, 915 (2009).

[7] W. Münzer, A. Neubauer, T. Adams, S. Mühlbauer, C. Franz, F. Jonietz, R. Georgii, P. Böni, B. Pedersen, M. Schmidt, A. Rosch, and C. Pfleiderer, Skyrmion lattice in the doped semiconductor $Fe_{1-x}Co_xSi$, Phys. Rev. B **81**, 041203(R) (2010).

[8] H. Wilhelm, M. Baenitz, M. Schmidt, U. K. Rößler, A. A. Leonov, and A. N. Bogdanov, Precursor Phenomena at the Magnetic Ordering of the Cubic Helimagnet FeGe, Phys. Rev. Lett. **107**, 127203 (2011).

[9] S. Seki, X. Z. Yu, S. Ishiwata, and Y. Tokura, Observation of skyrmions in a multiferroic material, Science **336**, 198 (2012).

[10] Y. Tokunaga, X. Z. Yu, J. S. White, H. Rønnow, D. Morikawa, Y. Taguchi, and Y. Tokura, A new class of chiral materials hosting magnetic skyrmions beyond room temperature, Nat. Commun. **6**, 7638 (2015).

[11] S. Heinze, K. von Bergmann, M. Menzel, J. Brede, A. Kubetzka, R. Wiesendanger, G. Bihlmayer, and S. Blügel,

Skyrmion phase and competing magnetic orders on a breathing kagome lattice, Nat. Phys. **7**, 713 (2011).

[12] C. Moreau-Luchaire, C. Moutafis, N. Reyren, J. Sampaio, C. A. F. Vaz, N. Van Horne, K. Bouzehouane, K. Garcia, C. Deranlot, W. P., P. Wohlhüter, J.-M. George, M. Weigand, J. Raabe, V. Cros, and A. Fert, Additive interfacial chiral interaction in multilayers for stabilization of small individual skyrmions at room temperature, Nat. Nanotechnol. **11**, 444 (2016).

[13] A. Soumyanarayanan, M. Raju, A. L. Gonzalez Oyarce, A. K. C. Tan, M.-Y. Im, A. P. Petrovic, P. Ho, K. H. Khoo, M. Tran, C. K. Gan, E. F., and C. Panagopoulos, Tunable room-temperature magnetic skyrmions in Ir/Fe/Co/Pt multilayers, Nat. Mater. **16**, 898 (2017).

[14] T. Kurumaji, T. Nakajima, M. Hirschberger, A. Kikkawa, Y. Yamasaki, H. Sagayama, H. Nakao, Y. Taguchi, T. Arima, and Y. Tokura, Skyrmion lattice with a giant topological Hall effect in a frustrated triangular-lattice magnet, Science **365**, 914 (2019).

[15] M. Hirschberger, T. Nakajima, S. Gao, L. Peng, A. Kikkawa, T. T. Kurumaji, M. Kriener, Y. Yamasaki, H. Sagayama, H. Nakao, K. Ohishi, K. Kakurai, Y. Taguchi, X. Yu, T. Arima, and Y. Tokura, Skyrmion phase and competing magnetic orders on a breathing kagome lattice, Nat. Commun. **10**, 5831 (2019).

[16] H. S. Park, X. Yu, S. Aizawa, T. Tanigaki, T. Akashi, T. Takahashi, K. Matsuda, N. Kanazawa, Y. Onose, D. Shindo, A. Tonomura, and Y. Tokura, Observation of the magnetic flux and three-dimensional structure of skyrmion lattices by electron holography, Nat. Nanotechnol. **9**, 337 (2014).

[17] Y. Okamura, F. Kagawa, S. Seki, and Y. Tokura, Transition to and from the skyrmion lattice phase by electric fields in a magnetoelectric compound, Nat. Commun. **7**, 12669 (2016).

[18] J. S. White, A. Butykai, R. Cubitt, D. Honecker, C. D. Dewhurst, L. F. Kiss, V. Tsurkan, and S. Bordács, Direct evidence for cycloidal modulations in the thermal-fluctuation-stabilized spin spiral and skyrmion states of GaV_4S_8, Phys. Rev. B **97**, 020401(R) (2018).

[19] M. N. Wilson, M. Crisanti, C. Barker, A. Štefančič, J. S. White, M. T. Birch, G. Balakrishnan, R. Cubitt, and P. D. Hatton, Measuring the formation energy barrier of skyrmions in zinc-substituted Cu_2OSeO_3, Phys. Rev. B **99**, 174421 (2019).

[20] A. Chacon, A. Bauer, T. Adams, F. Rucker, G. Brandl, R. Georgii, M. Garst, and C. Pfleiderer, Uniaxial Pressure Dependence of Magnetic Order in MnSi, Phys. Rev. Lett. **115**, 267202 (2015).

[21] Y. Nii, T. Nakajima, A. Kikkawa, Y. Yamasaki, K. Ohishi, J. Suzuki, Y. Taguchi, T. Arima, Y. Tokura, and Y. Iwasa, Uniaxial stress control of skyrmion phase, Nat. Commun. **6**, 8539 (2015).

[22] T. Nakajima, V. Ukleev, K. Ohishi, H. Oike, F. Kagawa, S. Seki, K. Kakurai, Y. Tokura, and T. Arima, Uniaxial-stress effects on helimagnetic orders and skyrmion lattice in Cu_2OSeO_3, J. Phys. Soc. Jpn. **87**, 094709 (2018).

[23] V. A. Sidorov, A. E. Petrova, P. S. Berdonosov, V. A. Dolgikh, and S. M. Stishov, Comparative study of helimagnets MnSi and Cu_2OSeO_3 at high pressures, Phys. Rev. B **89**, 100403(R) (2014).

[24] H. C. Wu, T. Y. Wei, K. D. Chandrasekhar, T. Y. Chen, H. Berger, and H. D. Yang, Physical pressure and chemical expansion effects on the skyrmion phase in Cu_2OSeO_3, Sci. Rep. **5**, 13579 (2015).

[25] I. Levatić, P. Popčević, V. Šurija, A. Kruchkov, H. Berger, A. Magrez, J. S. White, H. M. Rønnow, and I. Živković, Dramatic pressure-driven enhancement of bulk skyrmion stability, Sci. Rep. **6**, 21347 (2016).

[26] L. J. Bannenberg, R. Sadykov, R. M. Dalgliesh, C. Goodway, D. L. Schlagel, T. A. Lograsso, P. Falus, E. Lelièvre-Berna, A. O. Leonov, and C. Pappas, Skyrmions and spirals in MnSi under hydrostatic pressure, Phys. Rev. B **100**, 054447 (2019).

[27] M. Crisanti, N. Reynolds, I. Živković, A. Magrez, H. M. Rønnow, R. Cubitt, and J. S. White, *In situ* control of the helical and skyrmion phases in Cu_2OSeO_3 using high-pressure helium gas up to 5 kbar, Phys. Rev. B **101**, 214435 (2020).

[28] X. Z. Yu, N. Kanazawa, Y. Onose, K. Kimoto, W. Z. Zhang, Y. Matsui, and Y. Tokura, Near room-temperature formation of a skyrmion crystal in thin-films of the helimagnet FeGe, Nat. Mater. **10**, 106 (2011).

[29] M. T. Birch, R. Takagi, S. Seki, M. N. Wilson, F. Kagawa, A. Štefančič, G. Balakrishnan, R. Fan, P. Steadman, C. J. Ottley, M. Crisanti, R. Cubitt, T. Lancaster, Y. Tokura, and P. D. Hatton, Increased lifetime of metastable skyrmions by doping, Phys. Rev. B **100**, 014425 (2019).

[30] P. Milde, E. Neuber, A. Bauer, C. Pfleiderer, H. Berger, and L. M. Eng, Heuristic description of magnetoelectricity of Cu_2OSeO_3, Nano Lett. **16**, 5612 (2016).

[31] K. Karube, J. S. White, N. Reynolds, J. L. Gavilano, H. Oike, A. Kikkawa, F. Kagawa, Y. Tokunaga, H. M. Rønnow, Y. Tokura, and Y. Taguchi, Robust metastable skyrmions and their triangular-square lattice structural transition in a high-temperature chiral magnet, Nat. Mater. **15**, 1237 (2016).

[32] H. Oike, A. Kikkawa, N. Kanazawa, Y. Taguchi, M. Kawasaki, Y. Tokura, and F. Kagawa, Interplay between topological and thermodynamic stability in a metastable magnetic skyrmion lattice, Nat. Phys. **12**, 62 (2016).

[33] A. Štefančič, S. H. Moody, T. J. Hicken, M. T. Birch, G. Balakrishnan, S. A. Barnett, M. Crisanti, J. S. O. Evans, S. J. R. Holt, K. J. A. Franke, P. D. Hatton, B. M. Huddart, M. R. Lees, F. L. Pratt, C. C. Tang, M. N. Wilson, F. Xiao, and T. Lancaster, Origin of skyrmion lattice phase splitting in Zn-substituted Cu_2OSeO_3, Phys. Rev. Mater. **2**, 111402(R) (2018).

[34] K. D. Chandrasekhar, H. C. Wu, C. L. Huang, and H. D. Yang, Effects of Jahn-Teller distortion on the skyrmion stability of $(Cu_{1-x}Ni_x)_2OSeO_3$, J. Mater. Chem. C **4**, 5270 (2016).

[35] A. S. Sukhanov, P. Vir, A. S. Cameron, H. C. Wu, N. Martin, S. Mühlbauer, A. Heinemann, H. D. Yang, C. Felser, and D. S. Inosov, Increasing skyrmion stability in Cu_2OSeO_3 by chemical substitution Cu_2OSeO_3, Phys. Rev. B **100**, 184408 (2019).

[36] T. Reimann, A. Bauer, C. Pfleiderer, P. Böni, P. Trtik, A. Tremsin, M. Schulz, and S. Mühlbauer, Neutron diffractive imaging of the skyrmion lattice nucleation in MnSi, Phys. Rev. B **97**, 020406(R) (2018).

[37] E. M. Forgan, S. J. Levett, P. G. Kealey, R. Cubitt, C. D. Dewhurst, and D. Fort, Intrinsic Behavior of Flux Lines in Pure Niobium near the Upper Critical Field, Phys. Rev. Lett. **88**, 167003 (2002).

[38] C. D. Dewhurst, GRASP User Manual, Technical Report No. ILL03DE01T, Institut Laue-Langevin, Grenoble (2003), www.ill.fr/lss/grasp.

[39] T. Pirling, G. Bruno, and P. J. Withers, SALSA - A new instrument for strain imaging in engineering materials and components, Mater. Sci. Eng. A **437**, 139 (2006).

[40] D. Richard, M. Ferrand, and G. Kearley, Analysis and visualisation of neutron-scattering data, J. Neutron Res. **4**, 33 (1996).

[41] B. Ouladdiaf, J. Archer, G. J. McIntyre, A. W. Hewat, D. Brau, and S. York, OrientExpress: A new system for Laue neutron diffraction, Physica B **385-386**, 1052 (2006).

[42] A. Tengattini, N. Lenoir, E. Andò, B. Giroud, D. Atkins, J. Beaucour, and G. Viggiani, NeXT-Grenoble, the neutron and x-ray tomography in Grenoble, Nucl. Instrum. Methods Phys. Res. A **968**, 163939 (2020).

[43] S. J. Clark, M. D. Segall, C. J. Pickard, P. J. Hasnip, M. I. J. Probert, K. Refson, and M. C. Payne, First principles methods using CASTEP, Z. Kristallogr. - Cryst. Mater. **220**, 567 (2005).

[44] J. P. Perdew, K. Burke, and M. Ernzerhof, Generalized Gradient Approximation Made Simple, Phys. Rev. Lett. **77**, 3865 (1996).

[45] H. Monkhorst and J. Pack, Special points for Brillouin-zone integrations, Phys. Rev. B **13**, 5188 (1976).

[46] A. Bauer and C. Pfleiderer, Magnetic phase diagram of MnSi inferred from magnetization and ac susceptibility, Phys. Rev. B **85**, 214418 (2012).

[47] M. T. Birch, S. H. Moody, M. N. Wilson, M. Crisanti, O. Bewley, A. Štefančič, G. Balakrishnan, R. Fan, P. Steadman, D. Alba Venero, R. Cubitt, and P. D. Hatton, Anisotropy-induced depinning in the Zn-substituted skyrmion host Cu_2OSeO_3, Phys. Rev. B **102**, 104424 (2020).

[48] J.-W. G. Bos, C. V. Colin, and T. T. M. Palstra, Magnetoelectric coupling in the cubic ferrimagnet Cu_2OSeO_3, Phys. Rev. B **78**, 094416 (2008).

[49] K. Karube, J. S. White, D. Morikawa, M. Bartkowiak, A. Kikkawa, Y. Tokunaga, T. Arima, H. M. Rønnow, Y. Tokura, and Y. Taguchi, Skyrmion formation in a bulk chiral magnet at zero magnetic field and above room temperature, Phys. Rev. Mater. **1**, 074405 (2017).

[50] D. Morikawa, X. Yu, K. Karube, Y. Tokunaga, Y. Taguchi, T.-h. Arima, and Y. Tokura, Deformation of topologically-protected supercooled skyrmions in a thin plate of chiral magnet $Co_8Zn_8Mn_4$, Nano Lett. **17**, 1637 (2017).

[51] T. Nakajima, H. Oike, A. Kikkawa, E. P. Gilbert, N. Booth, K. Kakurai, Y. Taguchi, Y. Tokura, F. Kagawa, and T. Arima, Skyrmion lattice structural transition in MnSi, Sci. Adv. **3**, e1602562 (2017).

[52] F. Kagawa, H. Oike, W. Koshibae, A. Kikkawa, Y. Okamura, Y. Taguchi, N. Nagaosa, and Y. Tokura, Current-induced viscoelastic topological unwinding of metastable skyrmion strings, Nat. Commun. **8**, 1332 (2017).

[53] A. Chacon, L. Heinen, M. Halder, A. Bauer, W. Simeth, H. Mühlbauer, S. Berger, M. Garst, A. Rosch, and C. Pfleiderer, Observation of two independent skyrmion phases in a chiral magnetic material, Nat. Phys. **14**, 936 (2018).

[54] K. Karube, J. S. White, V. Ukleev, C. D. Dewhurst, R. Cubitt, A. Kikkawa, Y. Tokunaga, H. M. Rønnow, Y. Tokura, and Y. Taguchi, Metastable skyrmion lattices governed by magnetic disorder and anisotropy in β-Mn-type chiral magnets, Phys. Rev. B **102**, 064408 (2020).

[55] R. I. Joseph and E. Schlömann, Demagnetizing filed in nonellipsoidal bodies, J. Appl. Phys. **36**, 1579 (1965).

[56] L. Peng, Y. Zhang, L. Ke, T.-H. Kim, Q. Zheng, J. Yan, X.-G. Zhang, Y. Gao, S. Wang, J. Cai, B. Shen, R. J. McQueeney, A. Kaminski, M. J. Kramer, and L. Zhou, Relaxation dynamics of zero-field skyrmions over a wide temperature range, Nano Lett. **18**, 7777 (2018).

[57] J. Wild, T. N. G. Meier, S. Pöllath, M. Kronseder, A. Bauer, A. Chacon, M. Halder, M. Schowalter, A. Rosenauer, J. Zweck, J. Müller, A. Rosch, C. Pfleiderer, and C. H. Back, Entropy-limited topological protection of skyrmions, Sci. Adv. **3**, e1701704 (2017).

[58] M. Crisanti, G. Balakrishnan, M. T. Birch, R. Cubitt, P. D. Hatton, S. Holt, S. H. Moody, A. Stefancic, and M. N. Wilson, Study of the metastable skyrmion lattice in $(Cu_{1-x}Ni_x)_2OSeO_3$, Institut Laue-Langevin (ILL), 2019, doi: 10.5291/ill-data.5-42-489.

[59] R. Cubitt and M. Crisanti, Complimentary measurements on Cu_2OSeO_3, Institut Laue-Langevin (ILL), 2020, doi: 10.5291/ill-data.easy-571.

[60] R. Cubitt, S. Cabeza, M. crisanti, U. Oji, Investigating the strain profile in the Skyrmion phase of Ni doped $CuOSeO_3$, Institut Laue-Langevin (ILL), doi: 10.5291/ill-data.dir-188.